CHALMERS
UNIVERSITY OF TECHNOLOGY

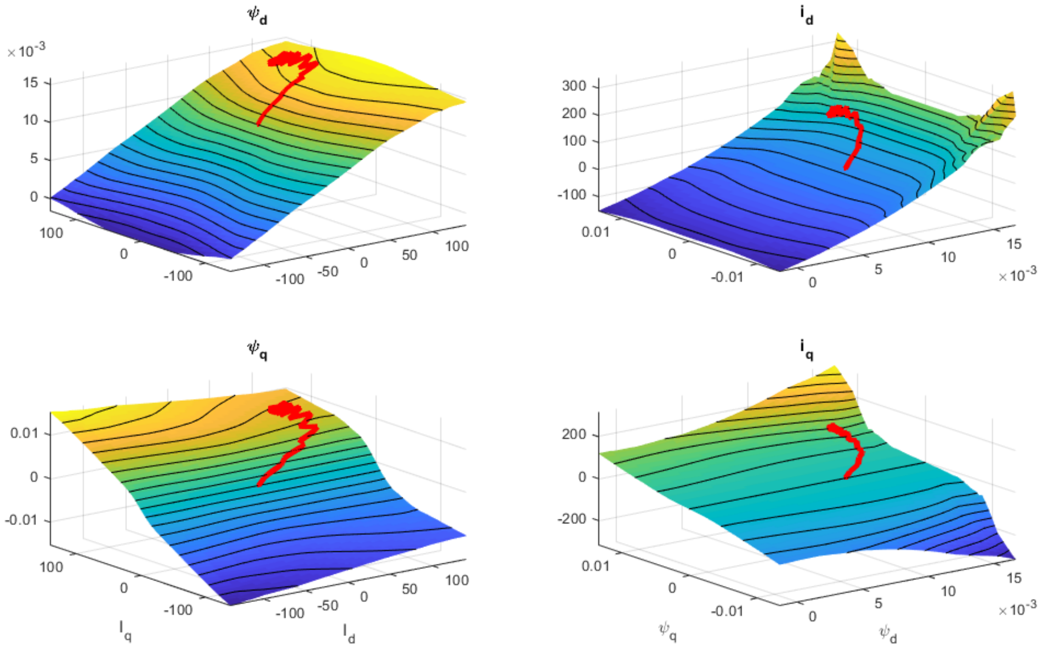

FEA-based Modelling of an Interior Permanent Magnet Synchronous Machine

Flux-based model of an IPMSM covering magnetic non-linearities and Low Speed Estimation using mutual differential inductance

Master's thesis in Systems, Control and Mechatronics

OSKAR SJÖKVIST

Department of Electrical Engineering
CHALMERS UNIVERSITY OF TECHNOLOGY
Gothenburg, Sweden 2020

Master's thesis 2020

FEA-based Modelling of an Interior Permanent Magnet Synchronous Machine

Flux-based model of an IPMSM covering magnetic non-linearities and Low Speed Estimation using mutual differential inductance

OSKAR SJÖKVIST

Department of Electrical Engineering
Division of Electric Power Engineering
Chalmers University of Technology
Gothenburg, Sweden 2020

FEA-based Modelling of an Interior Permanent Magnet Synchronous Machine
Flux-based model of an IPMSM covering magnetic non-linearities and Low Speed Estimation using mutual differential inductance
OSKAR SJÖKVIST

Supervisor: Torbjörn Thiringer, Department of Electrical Engineering
Supervisor: Daniel Chädström, Aros Electronics AB
Examiner: Torbjörn Thiringer

Master's Thesis 2020
Department of Electrical Engineering
Division of Electric Power Engineering
Chalmers University of Technology
SE-412 96 Gothenburg
Telephone +46 31 772 1000

Cover: Current and flux visualization constructed in Matlab showing the flux and current path traces taken by the flux model subject to a several subsequent step inputs and signal injection.

Typeset in LaTeX
Printed by Chalmers Reproservice
Gothenburg, Sweden 2020

FEM-based Simulation of an Interior Permanent Magnet Synchronous Machine
Flux-based model of an IPMSM covering magnetic non-linearities
OSKAR SJÖKVIST
Department of Energy and Environment
Chalmers University of Technology

Abstract

Interior Permanent Magnet Synchronous Machines are durable, high power-density machines. The motor geometry due to magnet placement inside the rotors introduces salience, and high stator currents causes the magnetic flux within the motor to take non-conventional routes depending on saturation and rotor angle. This thesis investigates a recently introduced motor modelling technique which is able to model the highly non-linear motor behaviour of the stator currents by the use of Finite Element Analysis (FEA) and implements this model in a Simulink environment. The model is based on the flux flow in the motor, and FEA is used to create mappings of the flux flows in the rotor as functions of stator currents and rotor position. The flux model is evaluated against reality and FEA. It shares high likeliness to the FEA-generated results, with a back-EMF peak error within 1 % and pulse response error maximum of 8 %. The flux model implementation is shown to be around 2 orders of magnitude faster at simulating dynamic motor behaviour than FEA, suggesting that it is an efficient way for accurate Simulation-in-the-Loop (SIL) development.

Further, the thesis introduces a signal injection technique considering non-zero mutual differential inductance and derives the exact response function of the direct-axis input voltage to quadrature-axis current for a square wave. It is shown that the conventional method of signal injection which assumed no mutual differential inductance will be offset from the real angular error by a phase scaling linearly with the mutual inductance term. Simulations using lookup tables for the instantaneous differential inductance in the mutual inductance model based estimator compared to a conventional estimator with constant direct- and quadrature-axis inductance show that the estimator implementation is at best a better choice in 47% of the cases. This could possibly be improved by basing the selection of inductance values on something other than the previous estimation. Otherwise, it might be beneficial to keep the low speed estimator simple.

Keywords: Finite Element Analysis (FEA / FEM), Interior Permanent Magnet Synchronous Machine (IPMSM / PMSM), Flux-based model, Saturation modelling, Simulation in the Loop (SIL), Low speed estimation (LSE), Signal injection, mutual differential inductance

Acknowledgements

First of all, I would like to thank Daniel Chädström for taking me in as my supervisor at Aros Electronics for his crucial guidance in this thesis work. I would like to thank Johan Åström and Mikael Alatalo at Aros Electronics as well for their guidance along the way as well as giving satisfying answers to all of my many questions during this thesis and availability for small talks without further notice. I would also really like to thank Simon Nilsson for connecting the dots between me and Aros, as well as everybody else I've met during my short but sweet time here. It has been a pleasure getting to know all of you Aros-people and I hope that we'll run into each other in the climbing gym soon again!
Lastly, I would also like to thank Torbjörn Thiringer for accepting me as his thesis student and guiding me towards reading up on electrical machines before doing a thesis work entirely encapsulated by the field "electrical machines".

Oskar Sjökvist, Gothenburg, February 2020

Contents

Glossary

EMF Electromotive Force. 6, 15, 16, 18, 24, 26, 33
EPMSM Exterior PMSM. 1

FEA Finite Element Analysis. 2, 6, 13, 16–18, 20, 24, 33

IPMSM Interior PMSM. 1, 6

LSE Low-Speed Estimator. 2, 6, 9, 10, 31, 33

MTPA Maximum Torque per Ampere. 18, 27–30

PMSM Permanent Magnet Synchronous Motor. 1–9, 33
PWM Pulse-Width Modulation. 2, 22, 24, 27

SIL Software-In-the-Loop. 2, 33

1
Introduction

In the dawn of electricity in modern society, electrical machines were on the menu for a new generation of automation. DC electrical motors allowed the manual labor force to relax while the machines allowed the envisioning of a utopia of tomorrow[1]. Now, many years later, the advent of cheap and highly effective computing, research and technological improvements has allowed for more advanced types of motors which can be tailored for almost any need. The Permanent Magnet Synchronous Motor (PMSM) is one of the newer generation of motors. This type of motor is required to be controlled using sophisticated software, and they have for a long time attracted ever increasing interest due to their high efficiency, reliability and high power density[2][3]. Within a PMSM there are strong permanent magnets, as the name implies. These are mounted on the rotor, and can be mounted either on the rotor surface or embedded into the iron core. Depending on the mounting, they are referred to as either an Interior PMSM (IPMSM) or an Exterior PMSM (EPMSM). This thesis treats the modelling of an IPMSM.

1.1 Background

Permanent Magnet Synchronous Motors build upon a simple concept: using magnets mounted on a shaft and electromagnets mounted around in a casing, it is possible to get movement by turning the electromagnets on and off in sequence. Since the key here is how the electricity in the wires are controlled, it is fairly straight-forward to apply some knowledge of Maxwell's equations on the motor interior and get a simple relationship between the angle of the rotor and when to turn an electromagnet on or off. When modelling PMSM motors, they are often linearized around some working point to simplify the model. This gives the model linear relationships between currents and voltages, in such a way that the iron in the model behaves linearly. This means that the iron does not magnetically saturate when the magnetic flux in the iron reaches high concentrations. Modelling the iron in this way means that the iron appears as an inductor in the corresponding electric schematic. It turns out that it is not difficult to create a simple machine model using a coupled linear differential equation under this assumption.[4]

However, modelling the iron as linear suffers the usual drawbacks of linearized models. While effective around certain working points it cannot be used to model broader and more detailed behaviour, or it is at the very least highly difficult to do so. Such behaviour include magnetic saturation, cogging torque, rotational asymmetry, iron loss, and non-perfect alignment of the rotor. [5][6][7]

In recent years this has become an interesting area of research and simulation for electrical engineers and scientists. Some are using newly acquired knowledge to expand on proper treatment of these phenomenon in modelling applications[8]. This has high potential value for a company specializing in electrical motor production, since a more accurate model yields a better development process and can be used to develop more accurate control algorithms.

1.2 Aim

The purpose of this project has two parts: first, it is meant to create a simulation environment for a model of an PMSM based on Finite Element Analysis (FEA) data mappings suitable for Software-In-the-Loop (SIL) development, taking magnetic saturation, cogging torque, and rotational asymmetry into account. This model will be called the *flux model*. Second, it is to introduce a sensorless Low-Speed Estimator (LSE) based on the FEA data mappings from the model, which will be called the *mutual inductance estimator*.

At the end of the project, the intention was to be able to show the results of simulations of a motor designed at Aros Electronics in test scenarios with high magnetic saturation and show the difference when accounting for non-linearities and comparing this to experimental measurements. The intention was also meant to show how the new LSE performs against a conventional sensorless LSE based on signal injection.

1.3 Scope

The project deals exclusively with interior permanent magnet synchronous motors, and will not try to apply anything onto other existing motor designs. Only the motor is of concern to this project, meaning that there will be no rigorous treatment of the corresponding current control system or Pulse-Width Modulation (PWM) of the input signal. The project is neither concerned with disturbed or noisy input signals, and will not treat these regions. Furthermore, the model will not discuss iron loss or imperfect rotor placement, or any other non-mentioned imperfection.

1.4 Ethical and Environmental aspects

This thesis project can be seen to abide by the United Nations Sustainable Development Goals number 8, 9, and 11[9]. If this thesis work is successful, it promotes economic growth by pushing the boundary of applied research forward directly at a respectable company. It also fosters further innovation for the same reason, as well as working towards a sustainable society by furthering work on electrical engines.

2
Theory

In this chapter, firstly the basics of PMSM modelling will be examined. After presenting a conventional linear model, the conventional way of signal injection is presented shortly. After that, the theory behind the flux model will be explained, and the theory behind the mutual inductance estimator will be developed.

2.1 Basics

2.1.1 Space vectors and coordinate transforms

A three-phase system is characterized by having three electrical AC currents which are out of phase at 120° from each other. These phases are called the *a-, b-* and *c-*phases of the system. Summing the phases together yields a result which optimally should be zero, however it can be shown that even if the result isn't zero, this so called zero-sequence component is in this application non-existent[4]. Since this also implies a constraint, this means that the system is in fact two-dimensional.

Each of the three phases correspond to a stator winding. In a Δ- or Y-connected motor, these windings are connected so it is useful to describe the system using the phase quantities u_a, u_b, u_c. As mentioned above, the system can be described by 2 coordinates instead of *abc*. These are usually called α and β respectively, and the zero-component can be left as a remainder denoted 0. The coordinate system is thus transformed from *abc*-coordinates using

$$\begin{bmatrix} u_\alpha \\ u_\beta \\ u_0 \end{bmatrix} = K \begin{bmatrix} \frac{2}{3} & -\frac{1}{3} & -\frac{1}{3} \\ 0 & \frac{1}{\sqrt{3}} & -\frac{1}{\sqrt{3}} \\ \frac{1}{2} & \frac{1}{2} & \frac{1}{2} \end{bmatrix} \begin{bmatrix} u_a \\ u_b \\ u_c \end{bmatrix} = T_{32} \begin{bmatrix} u_a \\ u_b \\ u_c \end{bmatrix} \tag{2.1}$$

where K is a scaling constant. In this thesis, $K = \sqrt{\frac{3}{2}}$, which is commonly called *power-invariant scaling.* Further on, when referencing current and voltages not given in *abc*-coordinates, the value is given using this scaling[1].

A motor is only useful once the rotor rotates, and to get it rotating it is necessary to create a torque. Since the only meaningful force generating torque is the one which pulls on the rotor magnetization, the direction of magnetization in the rotor is necessary to know. This means that it is useful to describe the motor in

[1] 1 Ampere in *abc* is thus not equal to 1 Ampere in $\alpha\beta$, and the same for Volt and Weber.

a coordinate system described by the rotor magnetization direction. In induction motors, the direction of magnetization does not correspond to the rotor position as the rotating magnetic flux rotates faster than the mechanical rotor[10]. This is not the case for PMSMs, as the permanent magnets mounted inside the rotor enforce a constant direction of rotor magnetization in relation to the rotor position.

The coordinate system used to describe the magnetization direction is the *dq*-coordinate system, which stand for *direct*- and *quadrature*-axis of the magnetization. The direct-axis is the direction of magnetization, and the quadrature-axis is 90° electrical from this direction, i.e the q-axis lies in between positive and negative magnetization directions. The transform from the coordinate system $\alpha\beta$ to the rotating system is given by

$$\begin{bmatrix} u_d \\ u_q \\ u_0 \end{bmatrix} = \begin{bmatrix} \cos\theta & \sin\theta & 0 \\ -\sin\theta & \cos\theta & 0 \\ 0 & 0 & 1 \end{bmatrix} \begin{bmatrix} u_\alpha \\ u_\beta \\ u_0 \end{bmatrix} = T_{dq} \begin{bmatrix} u_\alpha \\ u_\beta \\ u_0 \end{bmatrix} \tag{2.2}$$

where θ is the angle from the α-direction to the positive rotor magnetization direction. This is given by $\theta = n\theta_r$ where n is the number of pole pairs and θ_r is the rotor position.

2.1.2 Conventional PMSM model

2.1.2.1 Non-salient model

For a conventional non-salient PMSM model, it is convenient to express the currents and voltages in complex coordinates which is readily done by dropping the zero-component. Then, these can be written in $\alpha\beta$ or dq as

$$u_s = u_d + ju_q = e^{-j\theta}(u_\alpha + ju_\beta) \tag{2.3}$$

The governing electrical equation of the PMSM in a static frame is

$$\vec{V}_s - R_s\vec{i}_s - \frac{\mathrm{d}\vec{\psi}_s}{\mathrm{d}t} = 0 \tag{2.4}$$

where $\vec{V}_s$ is the stator voltages, R_s is the stator resistance, $\vec{i}_s$ is the stator currents, and $\vec{\psi}_s$ is the stator flux linkages. By assuming that the stator flux linkage can be described by

$$\vec{\psi}_s = L_s\vec{i}_s + \vec{\psi}_r \tag{2.5}$$

where L_s is constant stator inductances and $\vec{\psi}_r$ is the rotor flux vector, it is possible to obtain the conventional non-salient PMSM model. In a static *abc* or $\alpha\beta$ reference frame, this model can be described as an RL-circuit in series with a voltage source, and since the rotor flux vector rotates with the rotor, $\vec{\psi}_r = \psi_r e^{j\theta}$. In future references in this thesis, vector notation is dropped.

It is beneficial to describe the model in a rotating *dq*-frame instead as this allows for an intuitive control of the torque-generating q-direction and ease of applying

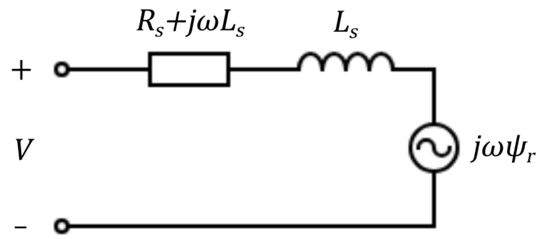

Figure 2.1: Schematic of a conventional non-salient PMSM model with constant inductances in a complex dq reference frame.

field-weakening. The drawback is that this also introduces another resistive term scaling with the angular velocity of the shaft due to the coordinate transformation. A schematic representation of the model can be seen in figure 2.1, and the governing equation becomes after dq-transformation

$$V = L_s \frac{\mathrm{d}i_s}{\mathrm{d}t} + (R_s + j\omega L_s)i_s + j\omega\psi_r. \tag{2.6}$$

2.1.2.2 Salient model

A salient PMSM model can be described as a motor which has a non-symmetrical rotor geometry along the angular direction. This means that the rotor will not be as easily magnetized in every direction, giving rise to different values for the inductance in the d and q directions. Modelling a salient PMSM requires leaving the convenient complex representation of the non-salient model in favor of a vector representation, as it is not possible to adequately model different inductance values in complex coordinates. Conceptually it is however still helpful to think of the model using the schematic in figure 2.1.

Modelling salience has pronounced effects on the motor, as it results in non-symmetrical current characteristics dependent on the rotor angle. It is possible to model this behaviour analytically[4], which after some simplifications result in the model equation

$$V_s = L_s \frac{\mathrm{d}i_s}{\mathrm{d}t} + (R_s\mathbb{I} + J\omega L_s)i_s + J\omega\Psi_r. \tag{2.7}$$

where $\mathbb{I}$ is the identity matrix, J is the equivalent vector representation of complex j, and the remaining values are represented in vector form and matrix form respectively,

$$J = \begin{bmatrix} 0 & -1 \\ 1 & 0 \end{bmatrix} \tag{2.8}$$

$$L_s = \begin{bmatrix} L_d & 0 \\ 0 & L_q \end{bmatrix} \tag{2.9}$$

$$\Psi_r = \begin{bmatrix} \psi_r \\ 0 \end{bmatrix}. \tag{2.10}$$

2.1.3 Low Speed Estimation by Signal Injection

If the PMSM motor is salient it is possible to estimate the rotor position without the use of a sensor. By injecting a high-frequency voltage, too high for the motor to generate any noticeable torque, it is possible to estimate the rotor position by measuring the current draw of the motor without affecting the motor performance. This is known as *signal injection*. By examining the salient motor equation in (2.7) and assuming negligible resistance and rotor speed it is possible to obtain a gain function from the voltage to the current given by

$$\hat{i}(s) = \frac{1}{s}\left(\frac{L_q + L_d}{2L_qL_d}\mathbb{I} + \frac{L_q - L_d}{2L_qL_d}\begin{bmatrix}\cos 2\tilde{\theta} & \sin 2\tilde{\theta} \\ \sin 2\tilde{\theta} & -\cos 2\tilde{\theta}\end{bmatrix}\right)\hat{V}(s) \tag{2.11}$$

where $\hat{V}$ and $\hat{i}$ are given in the coordinate system assumed to be the correct one, and $\tilde{\theta}$ being the difference between the assumed angle and the correct angle[4]. The mathematics behind this will be examined in section 2.3, which starts a derivation without assuming a negligible resistance or mutual inductance, and it is continued in appendix A.

By injecting a signal in only the assumed d-direction it's possible to get an angle estimate by measuring the current obtained in either the assumed d- or the assumed q-direction. The response in the assumed d-direction yields a constant term as well as an angle-dependent on, but the the response in the assumed q-direction only contain the angle dependent term. Therefore it is preferable to chose only the response in the assumed q-direction.

Assuming that the input signal is a square wave with amplitude V and measuring the peak-to-peak current, the error angle estimate becomes

$$\tilde{\theta} = \frac{1}{2}\arcsin\left(\frac{2\omega_e \Delta\hat{i}_q L_q L_d}{\pi V(L_q - L_d)}\right) \tag{2.12}$$

where ω is the angular frequency of the injected signal and $\Delta\hat{i}_q$ is the measured current difference. This LSE will be called the *conventional estimator*.

2.2 Flux based IPMSM model

IPMSM's are by default salient machines, since the magnets mounted within the iron rotors have a magnetic permeability comparable to air rather than iron[11]. As such, they are aptly described by the aforementioned salient PMSM model in section 2.1.2. However, that model fails at complex behaviours such as iron saturation effects, and it is not possible to model neither cogging torque nor non-sinusoidal back-Electromotive Force (EMF).

The use of PMSMs has been on the rise for a long time [2], and FEA is often used to accurately calculate the machine current characteristics[12][13]. However, the use of FEA to directly generate test results is a cumbersome process as it often takes a lot of time to produce results. This has called for more efficient methods of simulating the PMSM, and some approaches based on the flux characteristics of the machine has been suggested and tested[8][14]; by basing the characteristic behaviour on the flux dynamics rather than the current dynamics in the machine it is possible to create a model which incorporates most of the desired non-linear dynamics. In this section, this model is introduced and a mathematical foundation is mentioned to create a basis for the requirements on the flux characteristics in order to properly apply the model.

2.2.1 Bijective functions

A bijective function is a one-to-one mapping of a set called the domain onto another set called the codomain[15]. Assuming that a function

$$f : \mathbf{R}^2 \to \mathbf{R}^2$$

is bijective, then there exists an inverse such that

$$f^{-1}(f(x)) = x.$$

Investigation of the domain and the codomain of a function may reveal the bijective property over at least a subset of the domain. Now, also suppose that the domain and codomain of the function f is discrete. Then f represents the pointers between two lists of number pairs. The function is still bijective, meaning that $(x, y) \to (a, b)$ and $(a, b) \to (x, y)$. Therefore it is straightforward to organize these numbers either according to (x, y) or according to (a, b). If luck may have it, the discrete domain can be linearly interpolated and extrapolated so that the the number pairs in between any discrete points in the new domain are directed at unique number pairs between the corresponding codomain number pairs, yielding another bijective funtion

$$F : \mathbf{R}^2 \to \mathbf{R}^2$$

which is the interpolated function of the discrete function f.

2.2.2 Magnetic flux dependencies

In any PMSM motor, magnetic flux go through the stator teeth, past the air gap between the stator and rotor and into the rotor. Subsequently, the flux go through the rotor and back into the stator, but some leakage flux occur as well taking unintended paths[16]. Due to the saliency of the machine, the path taken by the flux is slightly different if the rotor is at a slightly different position, meaning that the flux density is dependent on the rotor angle. If the iron is saturated in different regions of the motor, the flux takes different paths as well[14].

Since the saturation is dependent on flux generated by currents going through the stator phases, the flux density can be seen as being dependent on the phase currents. This means that the flux ψ in the motor can be written

$$\psi = \begin{bmatrix} \psi_a \\ \psi_b \\ \psi_c \end{bmatrix} = \psi(\theta, i_d, i_q). \tag{2.13}$$

This can also be expressed in dq using the coordinate transforms in section 2.1.1, and will further on be expressed in that fashion.

2.2.3 Flux model

In this section, the principles of the flux model are described based on the knowledge obtained in previous sections as well as in [8]. Modelling the motor using fluxes directly as in (2.4) instead of assuming a flux linear in current yields the dq-frame motor equations

$$\frac{\mathrm{d}\psi_d}{\mathrm{d}t} = V_d - Ri_d - \omega_r \psi_q \tag{2.14}$$
$$\frac{\mathrm{d}\psi_q}{\mathrm{d}t} = V_q - Ri_q + \omega_r \psi_d \tag{2.15}$$
$$\psi_d = f(i_d, i_q, \theta) \tag{2.16}$$
$$\psi_q = g(i_d, i_q, \theta) \tag{2.17}$$
$$T = T(i_d, i_q, \theta) \tag{2.18}$$

where $f(i_d, i_q, \theta)$ and $g(i_d, i_q, \theta)$ are functions describing the flux characteristics of the modelled motor, and T is the torque generated by the motor. Assuming some constant θ and assuming that there are some scattered data points[2] (i_d, i_q), suppose that

$$\Psi_\theta(i_d, i_q) = \begin{bmatrix} \psi_d \\ \psi_q \end{bmatrix} \tag{2.19}$$

is a bijective mapping $(i_d, i_q) \rightarrow (\psi_d, \psi_q)$ for which interpolated values are also bijective. Then it is possible to find an inverse

$$\Psi_\theta^{-1}(\psi_d, \psi_q) = \begin{bmatrix} i_d \\ i_q \end{bmatrix} = \begin{bmatrix} i_{d,\theta}(\psi_d, \psi_q) \\ i_{q,\theta}(\psi_d, \psi_q) \end{bmatrix} \tag{2.20}$$

where the interpolated values for ψ_d and ψ_q have corresponding values for i_d and i_q. Inserting this into (2.14) - (2.15) and integrating yields

$$\psi_d = \int V_d - Ri_{d,\theta}(\psi_d, \psi_q) - \omega_r \psi_q \mathrm{d}t \tag{2.21}$$
$$\psi_q = \int V_q - Ri_{q,\theta}(\psi_d, \psi_q) + \omega_r \psi_d \mathrm{d}t. \tag{2.22}$$

Since the model has knowledge of the true rotor position θ, the flux-current mappings can be seen as a three dimensional mapping, and integration can be done by using a lookup table for the current based on the instantaneous flux and rotor position. Selection of the appropriate torque can also be done in a similar fashion. This way of modelling the PMSM yields a simple and computationally fast method of describing the motor[8].

[2] In practice, data of the flux-mappings can be acquired either by finite element analysis or by experimental measurements.

2.3 Mutual inductance modelling

The method of simulating a PMSM as described in the previous section is highly attractive in terms of simulation times, but analytically calculating response functions is made simpler by the use of an inductance model. In section 2.1.3 a method of estimating the error between assumed rotor position and actual rotor position was introduced. However, that Low-Speed Estimator assumed a machine without mutual inductance. By modelling the mutual inductance effects as a basis for another Low-Speed Estimator, it is shown that a mutual inductance term L_{dq} will have a noticeable effect on the response of an injected signal. This section introduces a model containing mutual inductance, and the following section derives a corresponding Low-Speed Estimator based on signal injection.

Suppose that there is no assumption made about the differential mutual inductance terms L_{dq} or L_{qd} being zero. This case of cross-magnetization effects has been investigated for different combinations of pole pairs and stator slots before, by [17][18]. Some, such as those two as well as [19] implies that the cross-coupling terms are not necessarily equal to each other, i.e $L_{dq} \neq L_{qd}$, however others [20] state that they can be highly similar if not exactly the same as well. In [21], an approach of calculating the inductance matrix from an *abc*-reference system to a *dq*-reference system is introduced, and it is shown that the differential mutual inductances are equal under the assumptions made in the article. This means that the mutual inductances could possibly be either different or not, however no further investigation is done here. In this thesis, calculations of the differential inductance matrix from flux and current values implies that the mutual inductance terms are similar in value, and as such a model assuming $L_{dq} = L_{qd}$ can be employed.

Under the assumption that the cross inductance terms are non-zero, the governing equation from (2.4) can be described in *dq* by

$$L_s \frac{\mathrm{d}i}{\mathrm{d}t} = V - (R + \omega_r J L_s)i - \omega_r J \Psi_R \tag{2.23}$$

where the differential inductance matrix is

$$L_s = \begin{bmatrix} L_d & L_{dq} \\ L_{qd} & L_q \end{bmatrix} = \begin{bmatrix} \frac{\partial \psi_d}{\partial i_d} & \frac{\partial \psi_d}{\partial i_q} \\ \frac{\partial \psi_q}{\partial i_d} & \frac{\partial \psi_q}{\partial i_q} \end{bmatrix}. \tag{2.24}$$

2.3.1 Signal injection using mutual inductance model

This section expands on the subject of estimating the rotor position in the low speed region introduced in section 2.1.3 by applying it in the mutual inductance model introduced above. Since the estimator is made for the low-speed region, ω_r can be assumed small such that

$$||\omega_r L_s||_2 << ||R_s||_2 \tag{2.25}$$

$$||\omega_r \Psi_R||_2 << ||R_s||_2. \tag{2.26}$$

Also assume that L_s is constant. Then (2.23) becomes

$$L_s \frac{\mathrm{d}i_s}{\mathrm{d}t} = V_s - R_s \mathbb{I} i_s \tag{2.27}$$

Entering the Laplace domain and rearranging terms yields a gain function from a voltage input u to a current output i as

$$i(s) = (R_s \mathbb{I} + sL_s)^{-1} u(s) \tag{2.28}$$

However, the exact rotor position is not known. The voltage is injected in what is assumed to be the correct dq-frame, at a rotor position $\hat{\theta}$, just as the current is measured at this position. Call the assumed correct frame the $\hat{d}\hat{q}$-frame. The relationship between the signal injected in the assumed frame $\hat{V}(s)$ and the system input signal $u(s)$ is then $\hat{V}(s) = e^{J\tilde{\theta}} u(s)$ where $\tilde{\theta}$ is the error angle $\tilde{\theta} = \theta - \hat{\theta}$. Completely analogously for the current measured in the assumed correct frame $\hat{\imath}(s)$, the response signal becomes

$$\hat{\imath}(s) = e^{J\tilde{\theta}} (R_s \mathbb{I} + sL_s)^{-1} e^{-J\tilde{\theta}} \hat{V}(s) \tag{2.29}$$

This can be tediously calculated by hand, or simply and elegantly by using sophisticated software. Assuming that the signal $\hat{V}(s)$ is injected only in $\hat{d}$ and that $\hat{\imath}(s)$ is the response in $\hat{q}$, the gain function from $\hat{d}$ to $\hat{q}$ becomes

$$G_{dq}(s, \tilde{\theta}) = \frac{s(\frac{L_q - L_d}{2} \sin(2\tilde{\theta}) - L_{dq} \cos(2\tilde{\theta}))}{R^2 + R(L_d + L_q)s + (L_d L_q - L_{dq}^2)s^2}. \tag{2.30}$$

Neglecting R and L_{dq} in this equation yields the response function from $\hat{d}$ to $\hat{q}$ in the Low-Speed Estimator in (2.11). By replacing some terms in the gain function with constants and temporarily ignoring the values of these constants, the function reads

$$G_{dq}(s, \tilde{\theta}) = \frac{As}{a + bs + cs^2} \tag{2.31}$$

where the important factor is $A = A(\tilde{\theta})$. This factor contains information about the angle dependency of the response signal,

$$A = \frac{L_q - L_d}{2} \sin(2\tilde{\theta}) - L_{dq} \cos(2\tilde{\theta}). \tag{2.32}$$

Here is an interesting result. If there were no mutual inductance, then the cosine term in A would not exist, meaning that the amplitude of the error signal is offset by a phase scaling with the mutual inductance. Near $\tilde{\theta} = 0$, this term is constant, meaning that the Low-Speed Estimator assuming no mutual inductance will be offset by a constant term from the real error value unless the mutual inductance is zero. Another thing to note is that if $L_d - L_q = 0$ at the same time as $L_{dq} = 0$, it is not possible to obtain a low speed estimation since there will be no error signal amplitude.

An analytical expression for the response can be derived from here. For the case of a sine wave, it is straightforward to use $s = j\omega$, however it is useful to derive it for the case of a square wave. The derivation can be found in appendix A. The angle error estimate becomes:

$$\tilde{\theta} = \frac{1}{2}\arcsin\left(\frac{\Delta\hat{i}_q c(C_2 - C_1)(1 + e^{-C_1\tau})(1 + e^{-C_2\tau})}{4KV(e^{-C_1\tau} - e^{-C_2\tau})}\right) - \frac{\phi}{2} \tag{2.33}$$

$$C_1 = \frac{b}{2c} + \sqrt{\left(\frac{b}{2c}\right)^2 - \frac{a}{c}} \tag{2.34}$$

$$C_2 = \frac{b}{2c} - \sqrt{\left(\frac{b}{2c}\right)^2 - \frac{a}{c}} \tag{2.35}$$

$$K = \sqrt{\left(\frac{L_q - L_d}{2}\right)^2 + L_{dq}^2} \tag{2.36}$$

$$\phi = \arctan\left(\frac{-2L_{dq}}{L_q - L_d}\right) \tag{2.37}$$

$$a = R^2 \tag{2.38}$$

$$b = R(L_d + L_q) \tag{2.39}$$

$$c = (L_d L_q - L_{dq}^2) \tag{2.40}$$

where $\Delta\hat{i}_q$ is the measured peak-to-peak current in the assumed d-direction and V is the square wave amplitude.

3

Methods

3.1 Collection of flux versus current data

Collection of flux data was done by FEA-calculations of a modelled motor using Ansys Maxwell. The FEA-calculated points used for the model can be seen in the results section 4.1.1, and data was obtained for different i_d and i_q up to $I_{dq} = 125$ A, and θ_r for 360° at a resolution of 0.12° per step.

In order to obtain suitable lookup tables for the fluxes and torque, the data obtained from FEA was interpolated and extrapolated to a grid $-140 \leq I_d \leq 140$ A, $-140 \leq I_q \leq 140$ A, using a grid resolution of 5 A per step.

The angular resolution was set to 1.2° per step in the lookup tables. The reason for this was to increase the speed of the development and measurement process.

3.2 Specifications and design parameters of motor

Parameters of the motor used in measurements and in FEA are given in table 3.1, and a cross section of the motor can be seen in figure 3.1.

3.3 Model generation

3.3.1 Flux model

The flux model was implemented in Simulink using 3d lookup tables for flux mappings. The selected currents were then fed back into the flux model, repeating the process. 3d lookup tables were used for torque mappings as well, selecting torque based on current. The data obtained by FEA was used to generate the flux and torque mappings consisting of interpolated and extrapolated values for each electrical angle θ of the rotor. After the generation of flux surfaces in d and q, these surfaces were paired together creating a set of vectors for each θ, linking each pair (ψ_d, ψ_q) to a respective pair (i_d, i_q). The mappings were inspected and if found to be a bijection, the data pairs were flipped to create a mapping from (i_d, i_q) to (ψ_d, ψ_q) instead. These pairs were used as a basis for interpolation and extrapolation of

Motor parameter	Value
Stator diameter	72 mm
Stator length	30 mm
Air gap	0.5 mm
Stator windings	22
Stator resistance	0.0285 Ω
Stator teeth	6
Pole pairs	2
Tooth width	8.7 mm
Yoke	7 mm
Rotor diameter	36 mm
Rotor bridge	0.9 mm
Rotor rib	2.4 mm
Magnets	3.4×16 mm NdFeB38SH
Lamination	M310-50A

Table 3.1: Parameter specification for motor used in experiments and for FEA-data acquisition.

values for the current in and around the region for which there were FEA-data as functions of the magnetic flux.

3.3.2 Inductance table calculation

Inductance tables were created using the flux mappings according to a discrete equivalent to equation (2.24),

$$\frac{\partial \psi_a}{\partial i_b}[k] \approx \frac{\psi_a[k+1] - \psi_a[k-1]}{i_b[k+1] - i_b[k-1]} \tag{3.1}$$

where k is used as the lookup table index. In the case of mutual inductance, the differences in the dq and qd tables were investigated and found to be highly similar as will be seen in section 4.1.5. This supported that $L_{dq} = L_{qd}$, therefore the lookup table used for the mutual inductance estimator was the average of L_{dq} and L_{qd}.

3.4 Experimental measurements

The setup of the motor bench used for measurements can be seen in figure 3.2, using a Tektronix DPO3034 oscilloscope with Tek P6139a probes and a Voltcraft plus VSP 1410 HE power supply parallel coupled with three 2.2 mF capacitors. The control software and hardware used was supplied by Aros Electronics. Step-response measurements were made by locking the rotor in a position using a shaft-holding mechanism. In order to align the rotor to some specific direction, control software was used to force a current in a preset direction, forcing alignment of the d-direction to this position before the shaft-holding mechanism was used to lock the rotor in place. The obtained position was verified using a position encoder.

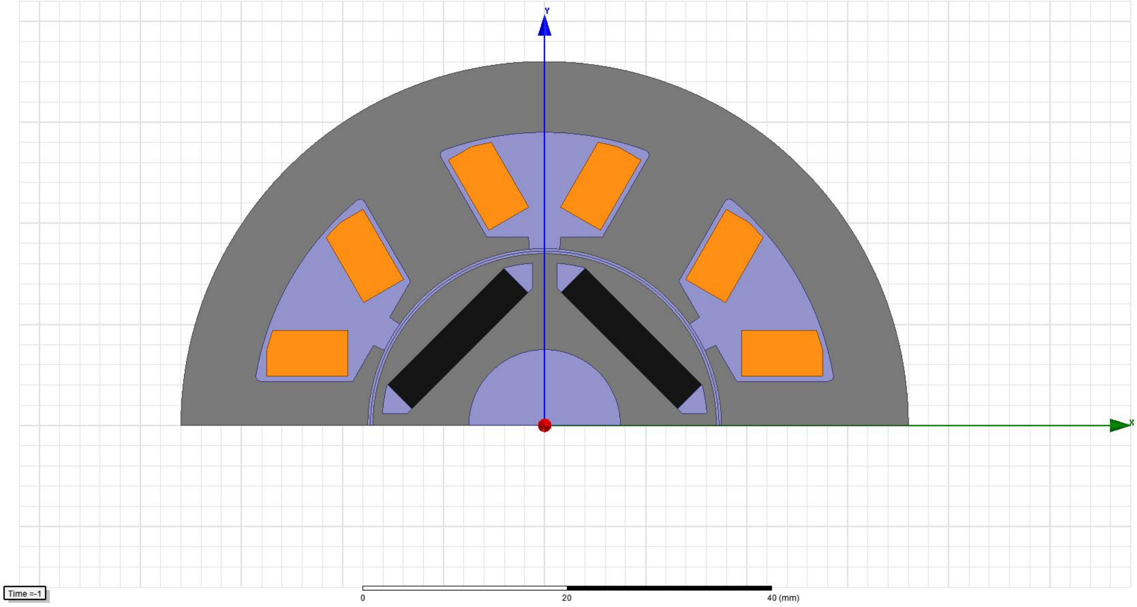

Figure 3.1: Cross section of motor used for measurement and FEA-calculations. Small grid lines are drawn at 2 mm distance, large grid lines at 10 mm.

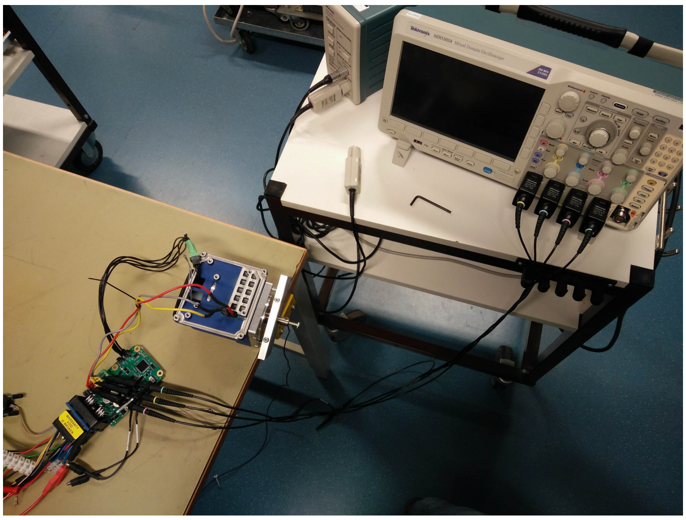

Figure 3.2: Motor bench used to obtain measurements. Not in picture: the screw-driver used for back-EMF measurements.

Back-EMF measurement was done using a AEG BS 12C2 screwdriver driven at around 10 Hz.

3.5 Model simulations

Simulations of the model were done by setting the angle of the rotor to a position and injecting pulses and steps corresponding to experimental measurements and FEA measurements. The results were compared against the corresponding measurements, and the results were analyzed.

The back-EMF generated by the model was calculated by setting the stator resistance to infinity and using no driving voltage. Since the back-EMF is the voltage generated at open circuit driving, in this case it is given by the time derivative of the flux as according to (2.14) and (2.15).

3.6 Base verification of model

3.6.1 Step response from FEA compared to model

FEA-data was generated to support the integrity of the flux based model. Step responses for the model were compared to FEA-simulations using voltage steps in positive and negative d-directions as well as in positive and negative q-directions. In the d-directions, the step amplitude was ± 7.35 V, and the results can be seen in figures 3.3a and 3.3b. In the q-directions, the step amplitude was ± 7.07 V, and the results can be seen in figures 3.3c and 3.3d.

In the d-directions, there is very good agreement between the FEA-simulations and the model, even in the extrapolated data-regions above 125 A. The q-directions also show very good agreement below 125 A, however the extrapolated areas doesn't feature a nearly as good match as the d-directions, which could possibly be explained by the q-direction being a less linear region than the d-direction outside the region of sampled data.

Another prevalent feature is the difference occurring after start. This is possibly due to a low resolution FEA-measurement, as the step time used was 145μs. The maximum discrepancy was around 8 % in the interpolated region.

3.6.2 Back-EMF measurement

FEA-simulations also resulted in back-EMF measurements, which can be seen in figure 3.4. The back-EMF is highly non-sinusoidal, and contain a lot of harmonic content. The curve agrees strongly with the back-EMF generated by the model which can be seen in figure 4.9d, with peak value agreement within 1%.

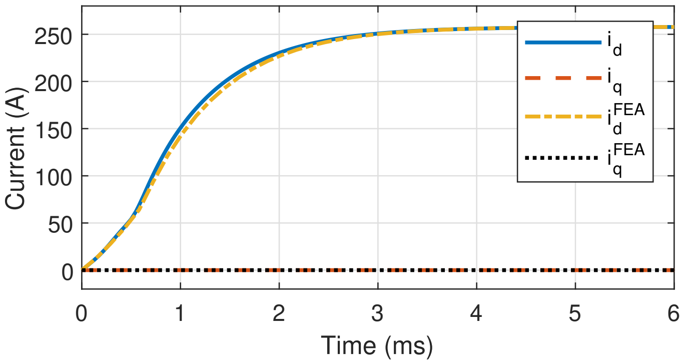

(a) Step response of model compared to that of FEA, using a step amplitude of 7.35 V injected in the d-direction.

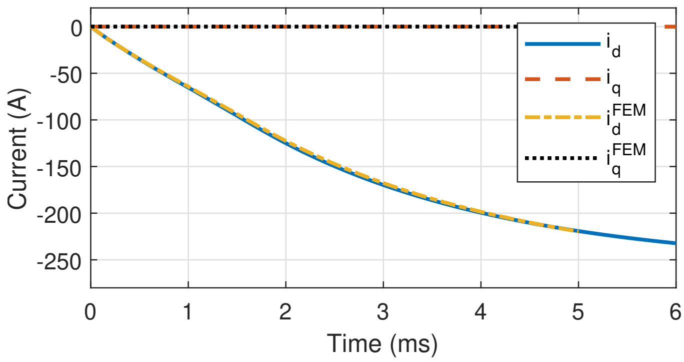

(b) Step response of model compared to that of FEA, using a step amplitude of -7.35 V injected in the d-direction.

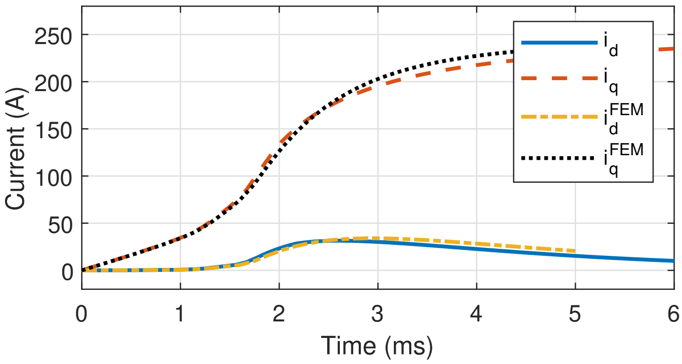

(c) Step response of model compared to that of FEA, using a step amplitude of 7.07 V injected in the q-direction.

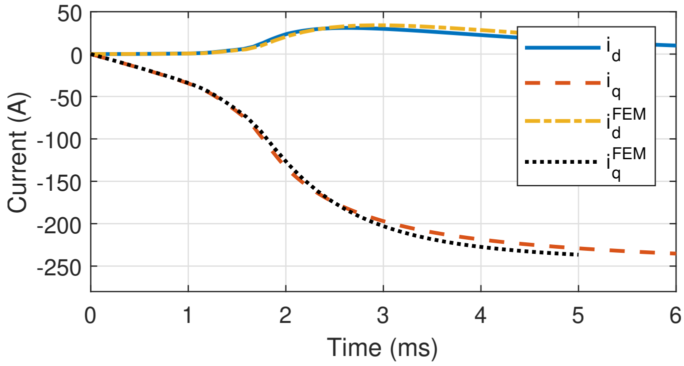

(d) Step response of model compared to that of FEA, using a step amplitude of -7.07 V injected in the q-direction.

Figure 3.3: Step responses of flux model compared to FEA.

3.6.3 Simulation time comparison

The time taken by the flux model implementation in Simulink for each pulse simulation was around 1 second using an 2.5 GHz Intel i5-3210M CPU. The corresponding simulation using FEA took around 5 minutes in Ansys Maxwell on an 3.5 GHz Intel Xeon E3-1246 CPU with an NVIDIA Quadro K2200 graphics card. These simulation times show that simulation of the flux model is significantly faster than calculating the motor response using FEA.

Overall, the comparison between the flux model and FEA results show that the model is in good agreement with the FEA-simulations, suggesting that the model is mostly limited by the accuracy of the FEA-data used to generate the model.

3.7 Signal injection comparison

The results from the mutual inductance estimator were compared to results of the conventional estimator. The conventional estimator working point was around

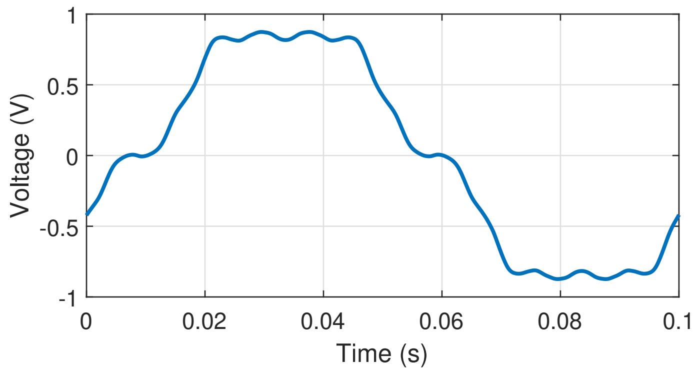

Figure 3.4: Back-EMF generated using FEA-simulation at 10 Hz electrical frequency.

$|I_{dq}| = 20$ A along the Maximum Torque per Ampere (MTPA) curve, using $L_d = 92\,\mu$H and $L_q = 186\,\mu$H. The results were divided into two parts: estimator errors along the MTPA curve, and some scattered current values. The MTPA measurements were futher divided into two different measurement sets: first, differential inductance lookup values were selected using the actual i_d, i_q and θ_r. This was done to validate the equations for the mutual inductance estimator and get a basis for the best possible performance of the mutual inductance estimator. Second, lookup values were selected using estimated i_d, i_q and θ_r, which is what would be done in real-life applications. The values for θ_r and $\tilde{\theta}$ used for verification were

$$\theta_r = 0°, 4°, ..., 60° \tag{3.2}$$

$$\tilde{\theta} = -30°, -28°, ..., 30° \tag{3.3}$$

and the estimator performance along the MTPA-curve was estimated using the average error over the span of rotor positions and angular errors, and the ratio of times it performed better than the conventional estimator. Estimator errors on the scattered points were only calculated by selecting inductance values based on estimated currents and angles.

4
Results

4.1 Model generation

4.1.1 FEA data points

Generating the data took ca 12 minutes per generated data point using Ansys Maxwell on a computer with an Intel Xeon E3-1246 CPU and NVIDIA Quadro K2200 graphics card. The points used to generate the data in this case can be seen in figure 4.1, and consist of around 1250 data points.

4.1.2 Generated flux surfaces

A few of the flux surfaces obtained for the model can be seen in figure 4.2a and 4.2b, which shows the surfaces for $\theta = 0$. The surfaces for each angle are similar in shape.

4.1.3 Generated current mappings

Inspecting the flux surfaces, it was noted that they were bijective. This allowed for the creation of the necessary current mappings. The current mappings for $\theta = 0$ can be seen in figures 4.3a and 4.3b.

4.1.4 Generated torque mappings

In order to procure a relevant torque mapping including cogging torque, a mapping from current to torque was made. One of these maps can be seen in figure 4.4, which shows the mapping for $\theta = 0$.

4.1.5 Differential inductance tables

Some differential inductance tables which were generated can be seen in figure 4.5a to 4.5d. Notice the likeness of figures 4.5b and 4.5c. Comparison of the corresponding non-extrapolated values of the surfaces reveal that the average difference is two orders of magnitude smaller than the largest value of the surfaces.

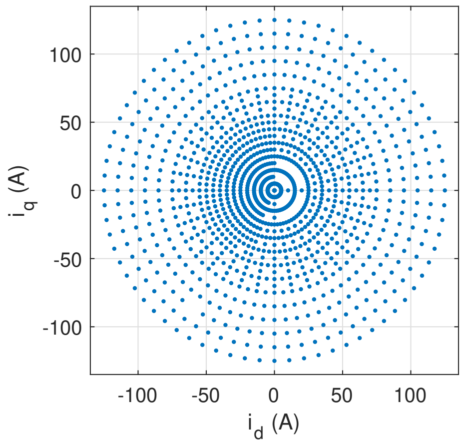

Figure 4.1: FEA data points used to generate appropriate model data. FEA data was generated up to currents of 125 A, while the data generated for the model extrapolated this to 140 A.

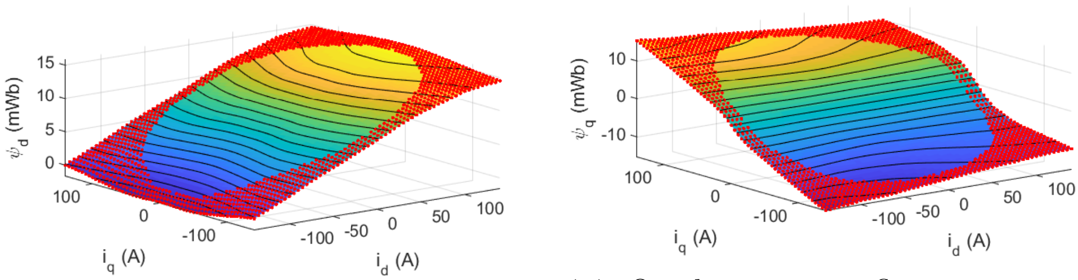

(a) Direct axis flux map interpolated and extrapolated from FEA-data for $\theta = 0$. Red dots mark extrapolated values.

(b) Quadrature axis flux map interpolated and extrapolated from FEA-data for $\theta = 0$. Red dots mark extrapolated values.

Figure 4.2: Flux mappings generated from FEA-data.

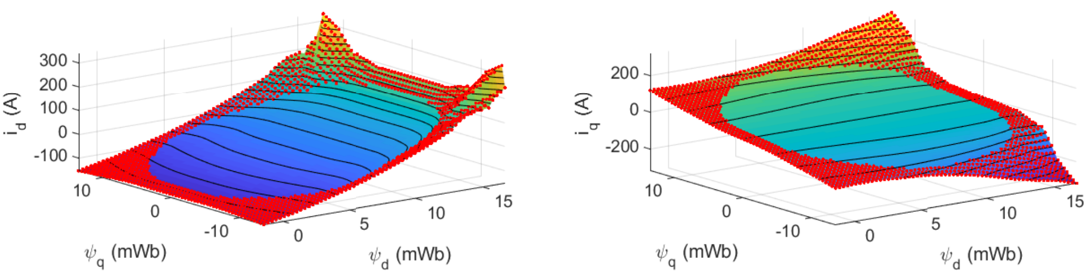

(a) Direct axis current map generated from FEA-data for $\theta = 0$. Red dots mark extrapolated values.

(b) Quadrature axis current map generated from FEA-data for $\theta = 0$. Red dots mark extrapolated values.

Figure 4.3: Current mappings generated from FEA-data.

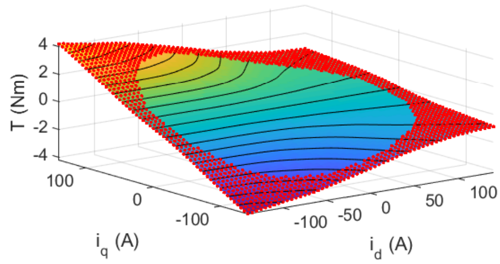

Figure 4.4: Torque map generated from FEA-data for $\theta = 0$. Red dots mark extrapolated values.

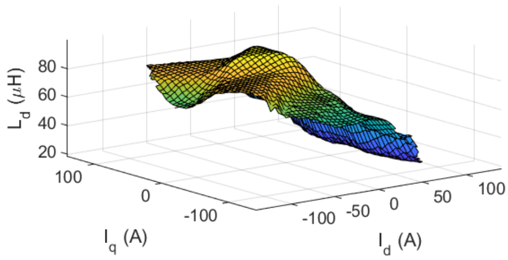

(a) Differential inductance L_d for $\theta = 0$.

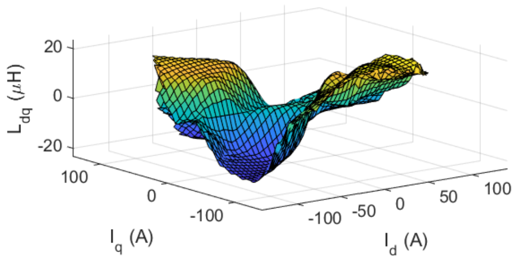

(b) Differential inductance L_{dq} for $\theta = 0$.

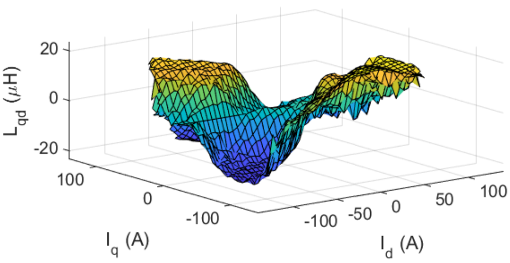

(c) Differential inductance L_{qd} for $\theta = 0$.

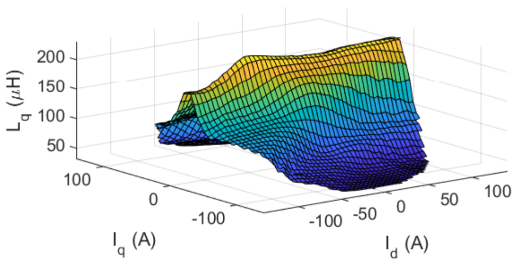

(d) Differential inductance L_q for $\theta = 0$.

Figure 4.5: Differential inductance calculated from flux data for $\theta = 0$. Extrapolated values are not shown to emphasis the likeness of L_{dq} and L_{qd}.

4.2 Flux model compared to experimental measurements

4.2.1 Pulse response from motor compared to model

Results from shorter pulse responses can be seen in figures 4.6a to 4.6d. The voltage pulse amplitudes were between 4.27 and 1.63 V, with pulse widths of 2.5 or 10 ms. In figures 4.6a and 4.6b, the current increase is faster in the model than in reality, which indicates that there is a lower effective inductance than in the motor. Thus, this suggests that there are some discrepancies between some of the parameters used to generate the data and reality. In figure 4.6d, a step response is shown after several measurements using a step amplitude of 1.77 V. Note that the steady state level of the real current is lower than predicted by the model. This can be explained by excessive use of the motor, resulting in a temperature increase of the stator resulting in an increased resistance. The resistance increases by about 4 percent per 10 °C [22]. This also very much highlights the importance of a correct temperature model of the resistance in an electrical machine in order to obtain highly accurate results, which is an area left untreated in this work. The other measurements were taken when the motor were at rated temperature.

In figure 4.6c the pulse response of the model is compared to the motor using a pulse amplitude of -1.63 V. There is good agreement on the rising edge, however on the falling edge the difference increases. This can be explained by the PWM dead time, which leaves the effective voltage at a non-zero value. Measurements of the PWM dead time and duty cycles leave the effective voltage at positive 0.14 V, and including this in the model shows improvements over previous results, see figure 4.7b.

Pulse response measurements were also done in positive and negative q-direction and two of these results can be see in figure 4.8a and 4.8b. These used a pulse amplitude of 1.83 V and a width of 10 ms. The current rises much slower than compared to the positive d-direction measurement. A last pulse measurement was made to examine if the model accurately depict the highly saturated response in the q-direction. The comparison between model and reality can be seen in figure 4.8c. An interesting thing to note is the behaviour of the d-current, which at high q-currents exhibits a peak. This is a behaviour which cannot possibly be explained by linear models, and it is therefore likely that this behaviour stem from saturation effects within the motor.

Another interesting phenomenon occurs at the end of the measured pulse, see figure 4.6e. The current abruptly stays at zero after reaching zero, which is possibly explained by inverter hardware implementation, with one likely candidate being that the current draw in a phase causes the deadtime voltage to be either positive or negative depending on whether the current is positive or negative. After reaching zero current draw in all phases, they would once again be symmetrical and thus drop from a prior non-zero effective voltage to zero.

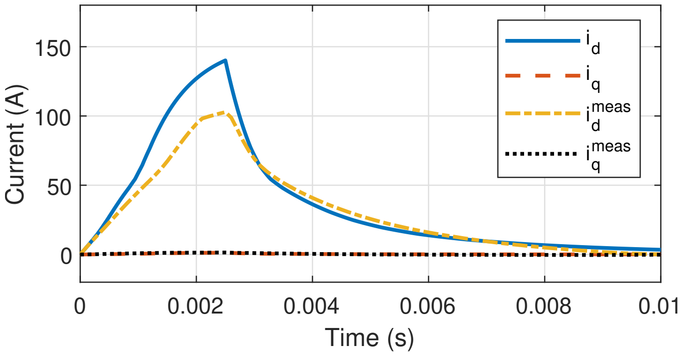

(a) Pulse response of model compared to that of the motor, using a pulse amplitude of 4.27 V and width 2.5 ms injected in the *d*-direction.

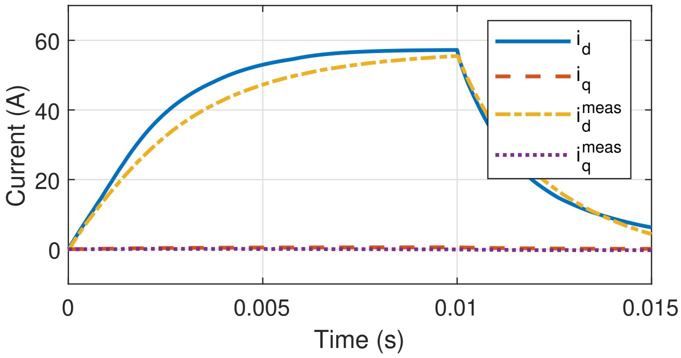

(b) Pulse response of model compared to that of the motor, using a pulse amplitude of 1.63 V and width 10 ms injected in the *d*-direction.

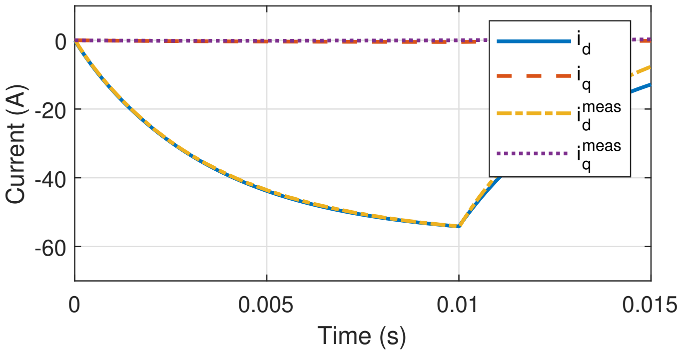

(c) Pulse response of model compared to that of the motor, using a pulse amplitude of -1.63 V and width 10 ms injected in the *d*-direction.

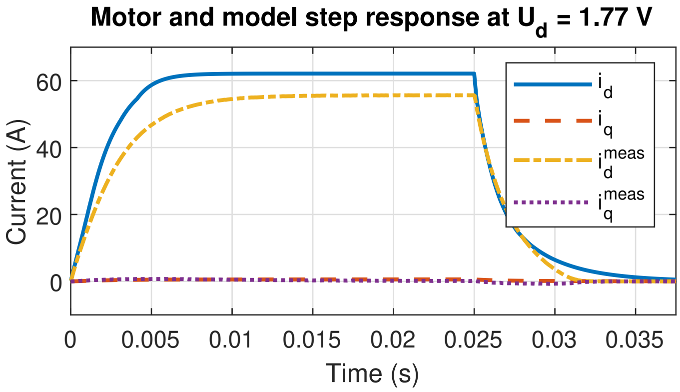

(d) Step response of model compared to that of the motor after excessive testing using a step amplitude of 1.77 V injected in the *d*-direction.

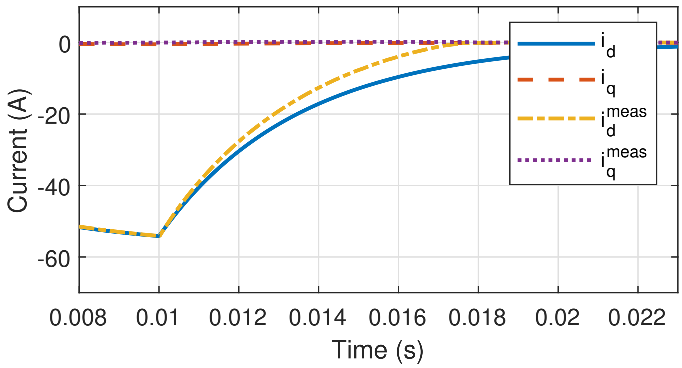

(e) Continuation of pulse from figure 4.6c.

Figure 4.6: Step- and pulse responses of flux model compared to motor using pulse injection in the *d*-direction.

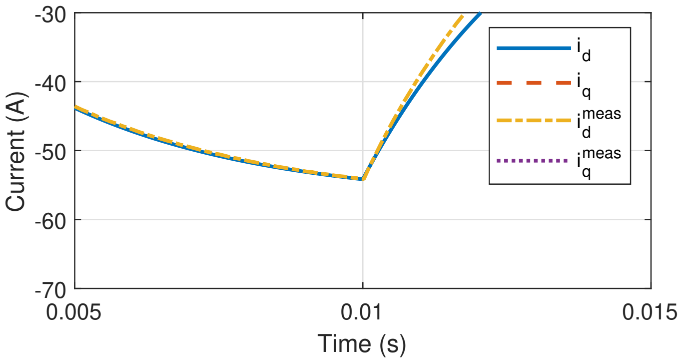

(a) Close-up of pulse from figure 4.6c.

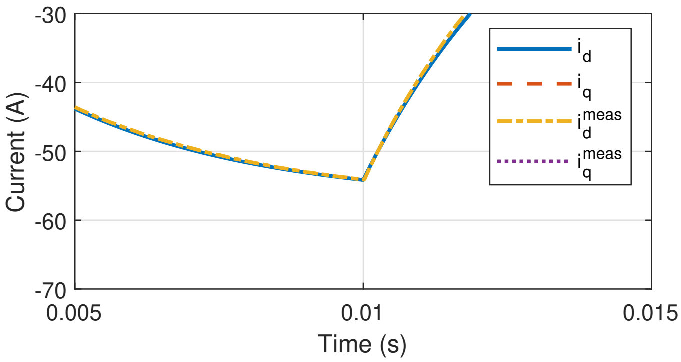

(b) Modified pulse response of model compared to that of the motor taking a simple PWM dead time into account leaving the effective post-pulse voltage at 0.14 V. The pulse had an amplitude of -1.63 V and width 10 ms, and was injected in the *d*-direction.

Figure 4.7: Comparison between pulse response modelling voltage occurring due to PWM dead time and no such modelling.

4.2.2 Back-EMF measurement

In figure 4.9a the measured phase-to-phase back-EMF is shown for an electrical frequency of about 10 Hz. As can be seen, this back-EMF is highly non-sinusoidal with lots of harmonic content. A close-up of this can be seen in figure 4.9c. The back-EMF has an amplitude of around 0.72 V, and reach several ”plateaus” during one revolution.

The phase-to-phase back-EMF of the model at a driving frequency of 10 Hz can be seen in figure 4.9b, and a closeup is seen in figure 4.9d. The model back-EMF amplitude is 0.87 V, and much like the motor reaches several ”plateaus” during one revolution which are characteristically alike apart from the level of noise as well as some visible symmetry in the model.

Considering the observed discrepancies between the motor and the model, observing lower inductance in positive d- as well as positive and negative q but strong agreement in negative d as well as a 20% difference in the back-EMF in the model compared to reality, it is possible that the magnet within the real motor is weaker than the magnet used in the simulated motor used to generate the FEA-data. This could possibly be due to magnet deterioration, rotor bridge modelling, motor lamination punching during the manufacturing process, or something else, however the cause of this is not investigated further in this thesis.

4.2.3 Large d-axis pulse response comparison

Due to limits in the power supply response time, the experimental measurement of the pulse response suffered a voltage drop. This was remedied by the PWM

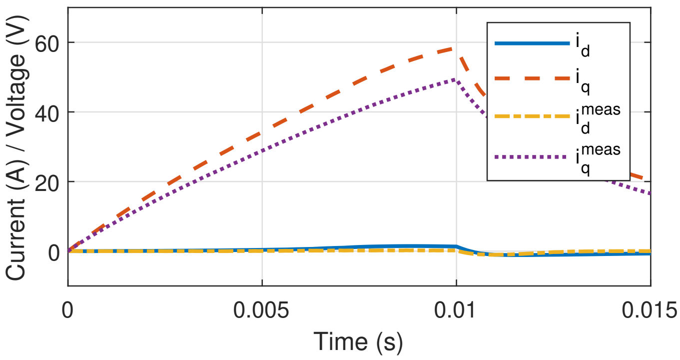

(a) Pulse response of model compared to that of the motor, using a pulse amplitude of 1.83 V and width 10 ms injected in the q-direction.

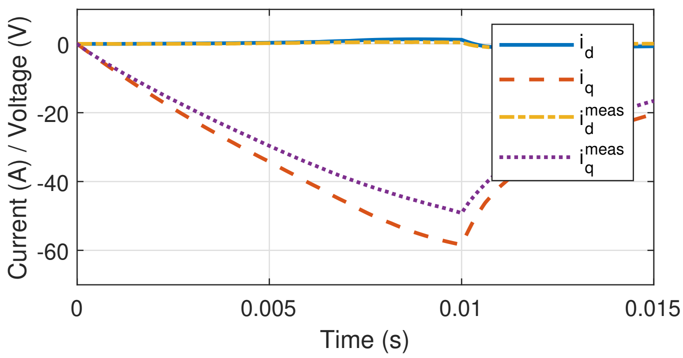

(b) Pulse response of model compared to that of the motor, using a pulse amplitude of -1.83 V and width 10 ms injected in the q-direction.

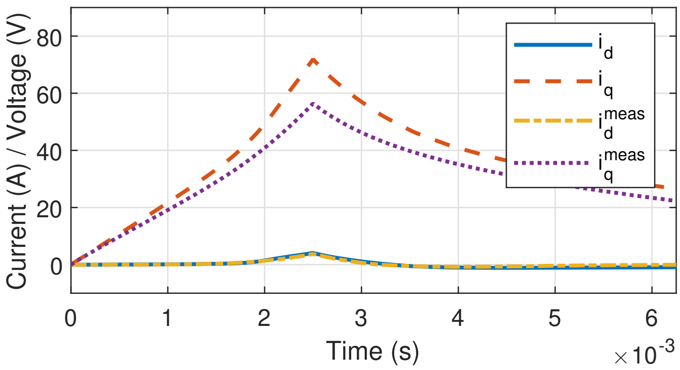

(c) Pulse response of model compared to that of the motor, using a pulse amplitude of 4.75 V and width 2.5 ms injected in the q-direction.

Figure 4.8: Step- and pulse responses of flux model compared to motor using pulse injection in the q-direction.

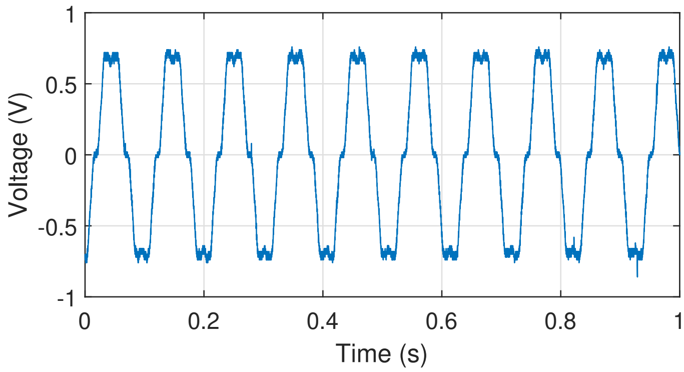

(a) Back-EMF of motor driven at ca 10 Hz electrical frequency.

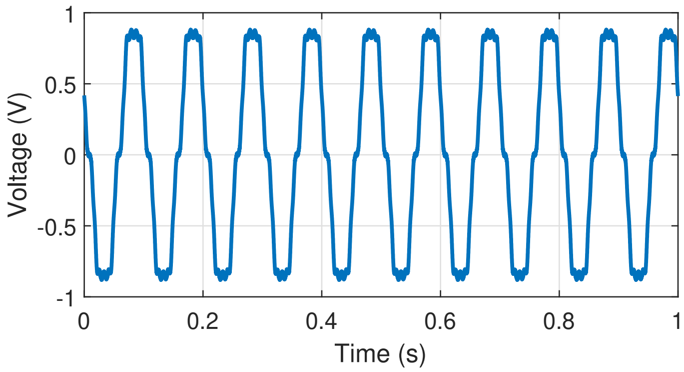

(b) Back-EMF generated by model driven at 10 Hz electrical frequency.

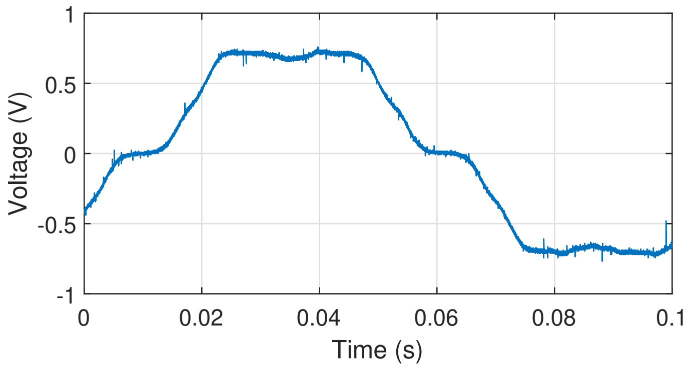

(c) Close-up of back-EMF of motor driven at ca 10 Hz electrical frequency.

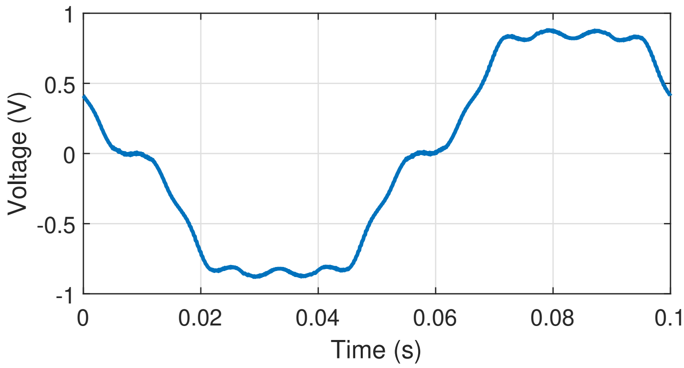

(d) Close-up of back-EMF generated by model driven at 10 Hz electrical frequency.

Figure 4.9: Back-EMF of model and motor.

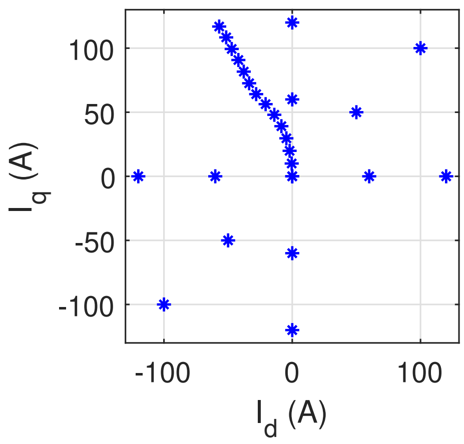

Figure 4.10: All current working points used for comparison between mutual inductance estimator and conventional estimator.

software, resulting in a slightly changing voltage output during the course of the pulse. The power supply voltage drop was from 20 Vdc to 16 Vdc during the course of the pulse. This resulted in lower a, b and c voltages, however the PWM controller successfully kept the voltage in dq, resulting in a small effective increase in d voltage. This data was obtained by measuring the phase voltages using an oscilloscope. The pulse response shown in figure 4.6a take this voltage drop into account, however it does not take actual PWM into account.

4.3 Estimator measurements and comparison

All points used for comparison between the mutual inductance estimator and the conventional one can be seen in figure 4.10. These points are further divided into two subcategories: the points along the MTPA-curve and a broader collection of points. The MTPA-curve is easily distinguished from the other points in the figure, curving into the 2nd quadrant at different phase amplitudes.

The MTPA-curve was calculated for a rotor angle of 0°. Different rotor angles result in slightly different curves. Signal injection was used with a voltage amplitude $V = 1$ V. This resulted in Δi_q on the order of 1 A, and a peak-to-peak d-current on the order of $\Delta i_d > 10$ A.

4.3.1 Estimator performances

For the MTPA curve measurements, the validation average error results can be seen in figure 4.11b, and the representative average error results can be seen in figure 4.11a. The performance of the estimator can be seen in figure 4.11c. The best average validation error for the mutual inductance estimator is 0.33° compared to the conventional estimator of 5.3°, however the best representative average error for the mutual inductance estimator was 8.0°. The best validation performance for the mutual inductance estimator was 0.99, but the best representative performance was

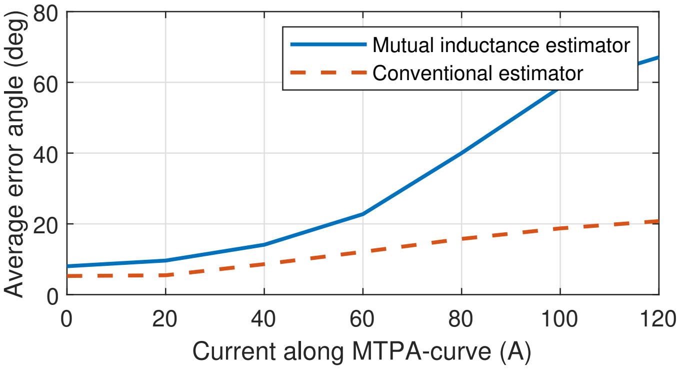

(a) Average error of estimator along MTPA-curve when differential inductance selection was based on estimated rotor angle.

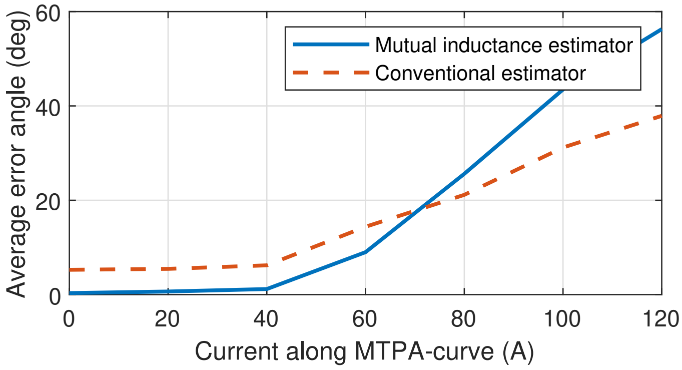

(b) Average error of estimator along MTPA-curve when differential inductance selection was based on precise rotor angle.

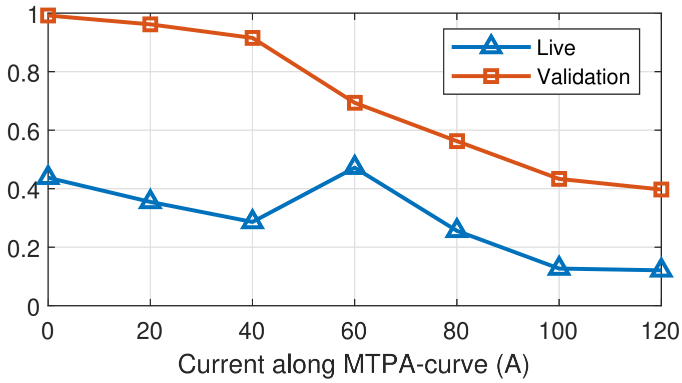

(c) Performance of advanced estimator compared to common estimator for some values along the MTPA-curve. The performance was measured as the ratio of cases for which the advanced estimator performed better than the common estimator.

Figure 4.11: Estimator comparisons for currents along MTPA-curve.

0.47 and the worst was 0.12.

The results for the non-MTPA points can be summarized as follows: Average estimator error for the mutual inductance estimator was (excluding 1 outlier) $15,5°$, and for the conventional estimator $25,8°$. The outlier was at $i_d = -100$ A, $i_q = -100$ A.

4.3.2 Regions of impossible measurements

As stated in section 2.3.1, if $L_q - L_d = 0$ while $L_{dq} = 0$, it is not possible to obtain an angle estimate. The whereabouts of these regions has been investigated for different rotor angles which can be seen in figure 4.12.
As can be seen in the figures, the area for which the signal disappear travels around the MTPA-curve several times each electrical rotation. Thus, if the estimation is off by around $\pm 10°$ the results from both estimators will be thrown off since the signal

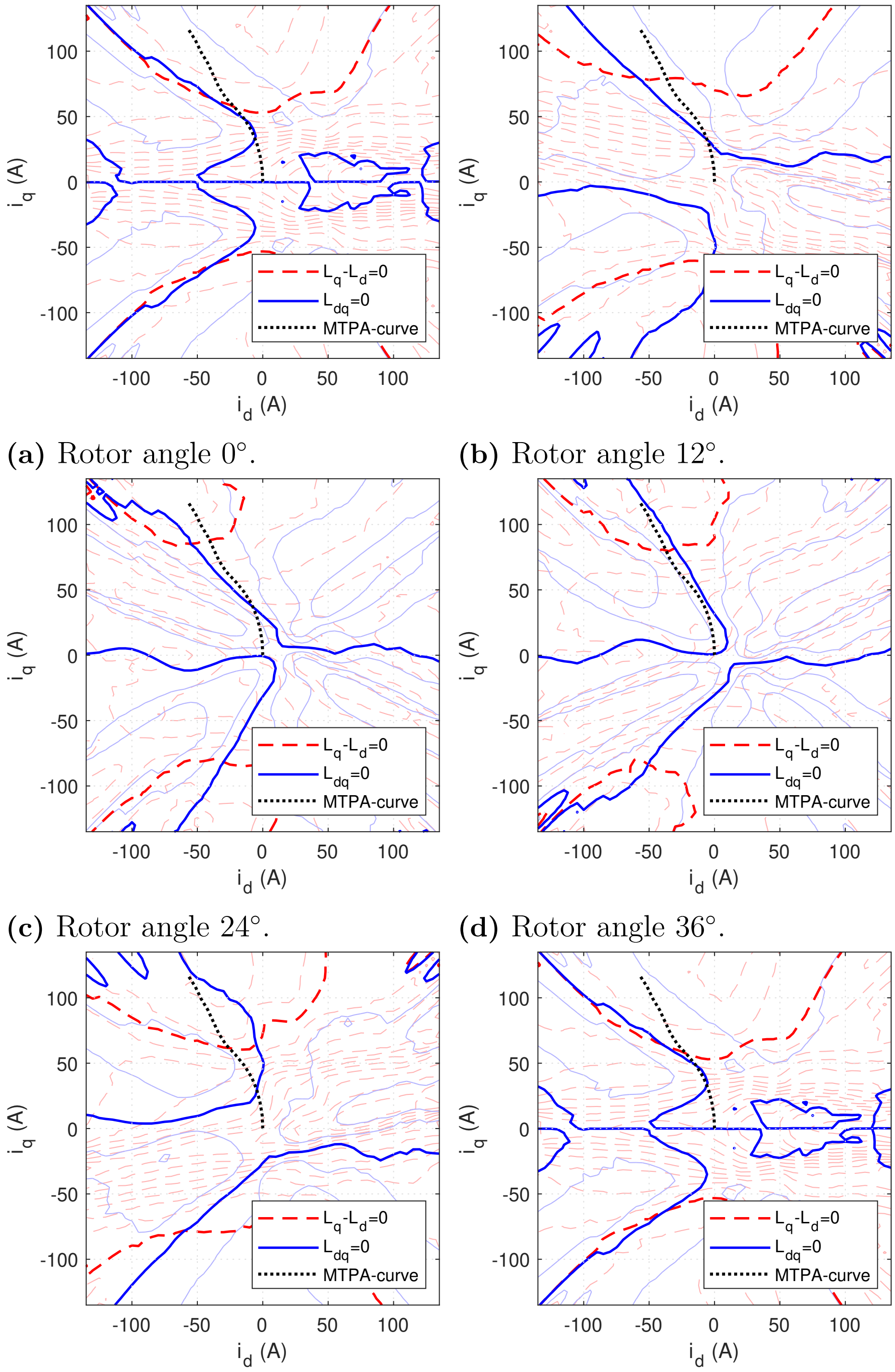

(a) Rotor angle 0°. **(b)** Rotor angle 12°.
(c) Rotor angle 24°. **(d)** Rotor angle 36°.
(e) Rotor angle 48°. **(f)** Rotor angle 60°.

Figure 4.12: Differential inductance lines for different rotor angles. Lines where $L_q - L_d = 0$ and $L_{dq} = 0$ are shown, as well as the MTPA-curve for $\theta = 0$. The isocurves for the differential inductance lines are shown at intervals of 15 μH.

disappear naturally in the region.

Since the mutual inductance estimator chose instantaneous differential inductance values based on the current estimation, it is likely that the chosen values are wrong and that the angle estimation is thrown off by sign differences in estimated and real $L_q - L_d$ and L_{dq}. This could explain the worse performance of the mutual inductance estimator over the range of MTPA points when running the representative tests. For the validation tests, it is clear that the mutual inductance estimator start falling off in its performance after 40 A but before 60 A. This correspond well with where the error signal amplitude become vanishing due to the differential inductance, see figure 4.12e-4.12f. Since the d-axis current shift by around 10 A, the differential inductance could vary greatly and even change signs during an injected signal period, however a constant value for the estimator was assumed.

Looking at the results for the non-MTPA points, the outlier lies in the extrapolated region. More importantly, the response signal amplitude drops to zero for some rotor angles for this point as the differential inductance reaches values for which there is no response signal, as can be seen in figure 4.12a. Considering that the result for the mutual inductance estimator is overall better than the conventional estimator for the non-MTPA points and that those points does not have completely vanishing response signals, it is likely that the error is due to differences in estimated and real differential inductance values. In order to obtain a better result using the mutual inductance estimator, a method of incorporating varying differential inductance would probably be useful.

4.4 Future research

Modelling of the motor the way it's used in this report suggest that it is an efficient way of simulating a model, however as mentioned earlier in this chapter, it is important to have a correct temperature model of the motor as well. This is something that has already been treated and implemented in [8], and can be added as a module to the model. It could be implemented as a module to this thesis model as well, and it would probably increase the accuracy of the model in the high speed region, an area which has been mostly left out.

When using signal injection to estimate the angular error of the motor, it could be beneficial to derive a response function factoring in the differential inductance as functions and not approximate these values as constants. The change in current draw in the d-direction when injecting a signal can be at least an order of magnitude larger than the change in the q-direction, meaning that the difference between the actual differential inductance values over the course of a signal injection period and the values used in the estimator could vary greatly.

The approximation that $L_{dq} = L_{qd}$ is something which is assumed due to measurements showing good agreement, and it can be argued that there should be a mutual differential inductance symmetry since it is a shared resource between the d-

and q-direction currents. However, the inductance overall is a material property and stems from the existence of microscopic regions of magnetization. This suggest that there might be more interesting phenomenons at work causing asymmetric mutual differential inductance curves, which could be investigated more deeply.

Lastly, another interesting route of improving the Low-Speed Estimator could be the implementation of a state machine taking the rotor position estimation into account in order to not use an ”easy” method of estimating the angle. The purpose of this would be to obtain a way of running one or a few iterations of rotor estimation which hopefully converges to the correct rotor position, or by using a live estimation of the motor parameters in order to get topical values for the differential inductance parameters.

5
Conclusion

A flux based model was implemented in Simulink and compared to FEA measurements and motor measurements. Comparison between FEA and the flux model show significant likeliness within 1 % peak back-EMF error, and the time taken by the Simulink model is two orders of magnitude faster than FEA. Discrepancies between the model and reality suggest that the data used to generate the model did not take certain effects into account, however all in all this suggests that the flux based model is an efficient and accurate way of modelling a PMSM limited only by the data used to generate the model. In conclusion, the model itself is highly attractive for a SIL development process. In future works implementing a flux based model, a suggestion for a data grid generated by FEA would consist of a 10-by-10 current grid in order to obtain a reasonable accuracy of the model compared to the time taken to generate the data.

A Low-Speed Estimator based on signal injection considering mutual inductance was also developed and tested against the flux based model. First, it was found that the existence of mutual inductance results in a non-zero response amplitude when at zero error angle. The mutual inductance estimator was found to be more accurate than a conventional estimator far from the regions where $L_q - L_d = 0$, with an average smaller estimator error of 10.3°. However, using the estimated position for inductance selection resulted in significantly poorer performance than the conventional estimator in regions where the response signal was vanishing, only outperforming the conventional estimator in at most 47 % of error angles and having a significantly larger average error. Conclusively, a simpler LSE is more useful if using a direct method of selecting inductance values, however it will be offset by a term linear in the mutual inductance of the motor. A more advanced estimator need to be developed to remedy this offset.

Bibliography

[1] James Hughes. Citizen cyborg. *Why democratic societies must respond to the redesigned human of the future*, 2004.

[2] Pragasan Pillay and Ramu Krishnan. Modeling of permanent magnet motor drives. *IEEE Transactions on industrial electronics*, 35(4):537–541, 1988.

[3] MS Merzoug and H Benalla. Nonlinear backstepping control of permanent magnet synchronous motor (pmsm). *International Journal of System Control*, 1(1):30–34, 2010.

[4] Lennart Harnefors. Control of power electronic converters and variable-speed drives. Compendium at Chalmers University of Technology.

[5] Wenyi Liang, Weizhong Fei, and Patrick Chi-Kwong Luk. An improved side-band current harmonic model of interior pmsm drive by considering magnetic saturation and cross-coupling effects. *IEEE Transactions on Industrial Electronics*, 63(7):4097–4104, 2016.

[6] Ki-Chan Kim. A novel method for minimization of cogging torque and torque ripple for interior permanent magnet synchronous motor. *IEEE Transactions on Magnetics*, 50(2):793–796, 2014.

[7] S Gair, A Canova, JF Eastham, and T Betzer. A new 2d fem analysis of a disc machine with offset rotor. In *Proceedings of International Conference on Power Electronics, Drives and Energy Systems for Industrial Growth*, volume 1, pages 617–621. IEEE, 1996.

[8] Xiao Chen, Jiabin Wang, Bhaskar Sen, Panagiotis Lazari, and Tianfu Sun. A high-fidelity and computationally efficient model for interior permanent-magnet machines considering the magnetic saturation, spatial harmonics, and iron loss effect. *IEEE Transactions on Industrial Electronics*, 62(7):4044–4055, 2015.

[9] United Nations. General Assembly et al. Resolution adopted by the general assembly on 25 september 2015. *Washington: United Nations*, 2015. available at: `https://www.refworld.org/docid/57b6e3e44.html` [Retrieved 2020-02-10].

[10] RW Davis. Notes on induction motor losses. *Proceedings of the American Institute of Electrical Engineers*, 32(2):363–367, 1913.

[11] Chengdu Heaven and Great Technology Co Ltd. Typical physical and chemical properties of some magnetic materials, 2020. `http://www.advancedmagnets.com/custom-magnets/` [Retrieved 2020-01-22].

[12] L Chang, AR Eastham, and GE Dawson. Permanent magnet synchronous motor: finite element torque calculations. In *Conference Record of the IEEE Industry Applications Society Annual Meeting,*, pages 69–73. IEEE, 1989.

[13] Fu Lin, Shuguang Zuo, Wenzhe Deng, and Shuanglong Wu. Modeling and analysis of electromagnetic force, vibration, and noise in permanent-magnet synchronous motor considering current harmonics. *IEEE Transactions on Industrial Electronics*, 63(12):7455–7466, 2016.

[14] Dakai Hu, Yazan M Alsmadi, and Longya Xu. High-fidelity nonlinear ipm modeling based on measured stator winding flux linkage. *IEEE Transactions on Industry Applications*, 51(4):3012–3019, 2015.

[15] Math Vault. The definitive glossary of higher mathematical jargon. `https://mathvault.ca/math-glossary/#otoc` [Retrieved 2020-01-22].

[16] Abdul Rehman Tariq, Carlos E Nino-Baron, and Elias G Strangas. Iron and magnet losses and torque calculation of interior permanent magnet synchronous machines using magnetic equivalent circuit. *IEEE transactions on magnetics*, 46(12):4073–4080, 2010.

[17] Lale T Ergene, Murat İmeryüz, and Cihad Ekin. Cross saturation inductance analysis of a permanent magnet synchronous motor. *Balkan Journal of Electrical and Computer Engineering*, 6(3):153–158, 2018.

[18] Bojan Stumberger, Gorazd Stumberger, Drago Dolinar, Anton Hamler, and Mladen Trlep. Evaluation of saturation and cross-magnetization effects in interior permanent-magnet synchronous motor. *IEEE Transactions on Industry Applications*, 39(5):1264–1271, 2003.

[19] Zheng Li and Hongmei Li. Mtpa control of pmsm system considering saturation and cross-coupling. In *2012 15th International Conference on Electrical Machines and Systems (ICEMS)*, pages 1–5. IEEE, 2012.

[20] Sebastian Ebersberger and Bernhard Piepenbreier. Identification of differential inductances of permanent magnet synchronous machines using test current signal injection. In *International Symposium on Power Electronics Power Electronics, Electrical Drives, Automation and Motion*, pages 1342–1347. IEEE, 2012.

[21] Markus Seilmeier and Bernhard Piepenbreier. Modeling of pmsm with multiple saliencies using a stator-oriented magnetic circuit approach. In *2011 IEEE International Electric Machines & Drives Conference (IEMDC)*, pages 131–136. IEEE, 2011.

[22] Åström J. Alatalo M. Chädström, D. Discussions, 2019-2020.

[23] Lennart Råde and Bertil Westergren. *Beta [beta] mathematics handbook*. Studentlitteratur, 2003.

A

Derivation of mutual inductance model response

Picking up where the theory-section left off,

$$G_{dq}(s,\tilde{\theta}) = \frac{As}{a+bs+cs^2} \tag{A.1}$$

$$A = \frac{L_q - L_d}{2}\sin(2\tilde{\theta}) - L_{dq}\cos(2\tilde{\theta}) \tag{A.2}$$

$$a = R^2 \tag{A.3}$$

$$b = R(L_d + L_q) \tag{A.4}$$

$$c = (L_d L_q - L_{dq}^2) \tag{A.5}$$

The square wave can be described as an infinite sum of step functions, where the relationship between the step length V_{step} and the square wave amplitude V_{amp} is $V_{step} = 2V_{amp}$. Denoting the step function with a step at τ as $H(t-\tau)$, a square wave $S(t)$ is obtained as

$$S(t) = -V_{amp} + \sum_{n=-\infty}^{\infty} (-1)^n V_{step} H(t - n\tau) \tag{A.6}$$

where τ is half the period time of the step function. The step response of the gain function given in equation (2.31) is obtained by multiplying the function with the Laplace transform of the step function, which is $H(s) = \frac{1}{s}$ at time zero:

$$G_{dq}(s,\tilde{\theta})H(s) = \frac{A}{a+bs+cs^2} = \frac{A}{c}\cdot\frac{1}{(s+C_1)(s+C_2)} \tag{A.7}$$

where the newly introduced constants C_1 and C_2 are obtained by completing the squares,

$$C_1 = \frac{b}{2c} + \sqrt{\left(\frac{b}{2c}\right)^2 - \frac{a}{c}} \tag{A.8}$$

$$C_2 = \frac{b}{2c} - \sqrt{\left(\frac{b}{2c}\right)^2 - \frac{a}{c}}. \tag{A.9}$$

Examining a lookup table [23] for the response yields that the system response to a single step function with unit amplitude with a step at $t = 0$ is

$$y(t) = \mathcal{L}^{-1}\left\{G_{dq}(s,\tilde{\theta})H(s)\right\}(t) = \begin{cases} \frac{A}{c}\cdot\frac{1}{C_2-C_1}\left(e^{-C_1 t} - e^{-C_2 t}\right), & \text{if } t > 0 \\ 0, & \text{otherwise} \end{cases} \tag{A.10}$$

The first thing to note is that the response tends towards zero. This can be explained by the fact that the steady state response should reasonably be zero, since the voltage input is in the d-direction and the output is in the q-direction.
Inserting this into (A.6) yields

$$\hat{i}_q(t) = \sum_{n=-\infty}^{\infty} (-1)^n V_{step} y(t - n\tau) \tag{A.11}$$

In order to obtain the peak-to-peak value $\Delta\hat{i}_q$, the current is sampled at $t = \tau$ and $t = 0$ and subtracted. Since the times are definite and the step function is zero if $t - n\tau < 0$, the summands become zero for all $n > 1$. By shifting index of summation and rearranging terms, followed by exchanging $n \to -n$, the expression for the peak-to-peak value become

$$\Delta\hat{i}_q = -2\frac{AV_{step}}{c(C_2 - C_1)}\left[\sum_{n=0}^{\infty}(-1)^n e^{-C_1\tau} - \sum_{n=0}^{\infty}(-1)^n e^{-C_2\tau}\right] \tag{A.12}$$

which is two geometric sums. Doing this last step yields a peak-to-peak value of

$$\Delta\hat{i}_q = 2\frac{AV_{step}}{c(C_2 - C_1)} \cdot \frac{e^{-C_1\tau} - e^{-C_2\tau}}{(1 + e^{-C_1\tau})(1 + e^{-C_2\tau})} \tag{A.13}$$

Now, looking at the factor A which contains an expression for $\tilde{\theta}$, it is interesting to obtain the definite expression for this. Introducing

$$A = K\sin(2\tilde{\theta} + \phi) \tag{A.14}$$

$$K = \sqrt{\left(\frac{L_q - L_d}{2}\right)^2 + L_{dq}^2} \tag{A.15}$$

$$\phi = \arctan\left(\frac{-2L_{dq}}{L_q - L_d}\right) \tag{A.16}$$

where arctan is implemented as the atan2-function and exchanging $V_{step} = 2V_{amp}$, the expression for the error angle estimate becomes

$$\tilde{\theta} = \frac{1}{2}\arcsin\left(\frac{\Delta\hat{i}_q c(C_2 - C_1)(1 + e^{-C_1\tau})(1 + e^{-C_2\tau})}{4KV_{amp}(e^{-C_1\tau} - e^{-C_2\tau})}\right) - \frac{\phi}{2} \tag{A.17}$$